Scattering Study of Single Charge Transfer in Ar^{q+} ($11 \leq q \leq 14$) on Ar Collisions at $72q$ eV

M. Sadilek, J. Vancura, and V. O. Kostroun*

Nuclear Science and Engineering Program, Ward Laboratory, Cornell University, Ithaca, New York 14853

Received: May 9, 1995[⊗]

Collisions of highly charged Ar^{q+} ions ($11 \leq q \leq 14$) with neutral Ar were investigated at $72q$ eV laboratory energy. Energy gain spectra were measured at different scattering angles, and relative doubly differential cross sections for the Ar$^{(q-1)+}$ product were obtained. Odd charge state projectiles are scattered with an energy gain corresponding to a narrow range of Q values, while even charge state projectiles are scattered with energy gains associated with three different groups of Q values. This even–odd variation with projectile charge state seems to be a general feature of Ar^{q+} on Ar scattering, but no explanation for this effect is offered at this time. Energy gain spectra measured at different scattering angles were integrated over scattering angles, and the resulting function, proportional to the Q value distribution function, reflects the density of capture states.

Introduction

Low-energy, highly charged ions have received considerable attention during the past decade. This attention stems from interest in the fundamental interactions of these ions with other atomic and molecular species and their role in astrophysical and laboratory thermonuclear fusion plasmas. The latter has considerable implications on practical applications of fusion research.

Collision spectroscopy provides important data on interparticle potentials as well as insight into the dynamics of elementary collision processes such as elastic and inelastic scattering, charge transfer, and reactive scattering.[1] A number of experiments on the scattering of low-energy, high-charge-state ions from various targets have been reported in the literature. A partial list of systems investigated includes the following: C^{4+} on He,[2–4] Ne^{4+}, N^{5+}, O^{6+}, F^{7+}, Ne^{8+} on He,[2] Ne^{q+} ($3 \leq q \leq 6$) on He,[5] N^{6+}, O^{6+} on He,[6] bare, hydrogen- and helium-like projectiles of C, N, O, and Ne on H$_2$ and rare gas targets,[7–9] and Ar^{6+} on He.[10–12]

A number of experiments have been carried out on the symmetric argon on argon system. These include measurements of forward-scattered ($\theta < 1°$) energy gain spectra and angular distributions in Ar^{4+} on Ar collisions for single and double electron capture,[13] energy gain spectra and differential cross sections in Ar^{5+} on Ar collisions,[14] and state-resolved angular distributions of single and double electron capture in Ar^{6+} on Ar collisions.[15,16] Angular distributions of projectiles that have undergone a particular energy gain were measured in coincidence with the final charge state of recoil ions for Ar^{q+} ($q = 8$, 9, and 11) on Ar collisions at $1.8q$ keV[17] and 12 keV.[18] With the exception of recent measurements of angular distributions in 50 keV Ar^{15+} on Ar collisions,[19] low or very low collision energy scattering data involving higher charge state q projectiles ($q \geq 10$) are quite scarce.[17,18,20] This is largely due to experimental difficulties associated with the production and transport of such species. Thus, not only does the intensity of the beam fall off rapidly with increasing charge state but the effect of space charge is much more severe for highly charged ion beams than for singly charged beams of the same velocity and intensity. In addition, the ions extracted from an ion source typically have an energy spread of a few electronvolts per charge. For some experiments, the primary beam has to be monochromatized with an attendant loss of beam intensity. The experimental situation is sometimes further complicated by the presence of ions with the same mass/charge ratio in the beam, such as Ar^{15+} and O^{6+}.

In a previous work,[21,22] we measured the energy gain spectra of low-energy Ar^{q+} ($8 \leq q \leq 14$) on Ar collisions at 0°. The spectra showed an even–odd variation, with even charge projectiles showing two distinct peaks and odd charge state projectiles showing only one peak in the energy gain spectra. In our scattering experiments,[20] we found that for Ar^{8+} and Ar^{10+} the two sharp peaks in the energy gain spectrum of the projectile which retains one electron after capture exhibit quite different angular distributions or scattering patterns. For the odd charge state projectiles, whose energy gain spectra show only one sharp peak, e.g. Ar^{9+} on Ar,[20,21] the angular distribution of scattered projectiles which retain only one electron is forward peaked. During the course of the investigation, the question arose as to how the higher Ar charge states behave as electrons are removed from the 2p shell. This paper presents results of a set of four scattering experiments in which Ar^{q+} ($11 \leq q \leq 14$) collided with neutral argon atoms at $72q$ eV projectile energy. Angular distributions and energy gain spectra at different scattering angles were recorded for projectiles which retained only one electron following the capture of one or more electrons from the target. The results are presented in the form of scattering contour maps, center-of-mass (c.m.) angular distributions, and Q value distributions.

Experimental Section

Metastable free, highly charged argon ions were produced by the Cornell superconducting solenoid cryogenic electron beam ion source (CEBIS)[23] and extracted at 2.33 kV. The ions were extracted from the source over a period of time lasting several milliseconds by the gradual lowering of the downstream electron-beam-ion-trap potential barrier. The extended extraction pulse then allowed single particle detection of the scattered ions. The ion charge state of interest was selected by a 90° bending magnet. The charge state selected ion beam, with a typical energy spread of $30-40q$ eV (fwhm), then entered the scattering chamber. The scattering apparatus is described in more detail elsewhere.[24] A brief description is given in Figure
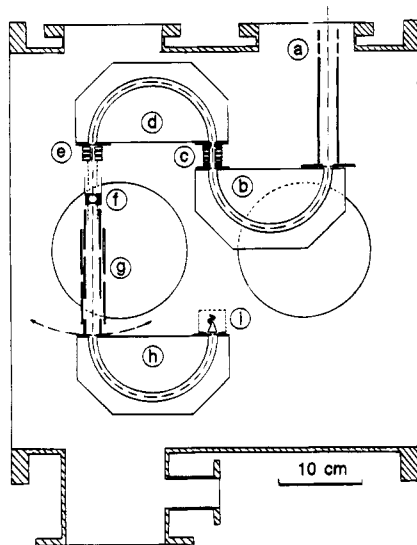
Figure 1. Experimental arrangement: (a) entrance einzel lens; (b) first 180° hemispherical analyzer (deflector); (c) decelerator ion optics; (d) monochromator; (e) exit einzel lens; (f) collision cell; (g) μ-metal shield; (h) movable analyzer; (i) channeltron electron multiplier.

1. The einzel lens (a) focused the ion beam into a 180° hemispherical electrostatic deflector (b). After deflection, the beam was slowed down by the deceleration lens (c) to the desired final energy. The beam then entered a 180° hemispherical electrostatic monochromator (d) with a $\Delta E/E$ of 0.005. After exiting the monochromator, the beam was focused by an einzel lens (e) onto the entrance slit of a 12-mm-long gas cell (f).

The target gas pressure in the cell ranged from 10^{-5} to 10^{-4} mbar and was determined from the rate of one-electron charge transfer in Ar^{q+} on Ar collisions whose absolute cross sections are known.[25] Upon exiting the cell, both the incident and charge-changed ions traversed a magnetically and electrically shielded drift region (g) to be energy analyzed by a third 180° hemispherical electrostatic analyzer (h) with a $\Delta E/E = 0.0033$. The ions were detected by a channeltron multiplier (i). The data acquisition and 180° hemispherical electrostatic analyzer potentials were controlled by an IBM PS/2 Model 30286 computer.

The energy and angular spread of the incident Ar^{q+} beam decelerated to the final energy were recorded, and the 0° laboratory scattering angle was determined prior to each scan. The energy gain spectra were obtained by varying the analyzer mean path potential (analyzer offset voltage V_{off}), while keeping the potential difference across the spherical electrodes (analyzer voltage V_A) constant. The fwhm of the primary beam was $0.42q$ eV, which corresponds to an overall $\Delta E/E$ of 0.0053. The angular distributions were obtained by moving the 180° spherical electrostatic analyzer along an arc whose radius is centered on the gas target cell. The angular spread was 0.48° or 8.4 mrad fwhm.

With target gas in the cell, the angular distribution data were recorded by setting the analyzer potentials to select a particular peak in the energy gain spectrum and then moving the analyzer along an arc. Each scan was repeated 3–5 times. The analyzer was then set to the next peak, and the procedure was repeated. From these angular distributions, the relative statistical weight of the product intensity scattered into a particular energy gain interval was determined.

Finally, energy gain scans at a fixed number of laboratory projectile scattering angles were measured. Both the angular and energy gain data were transformed into a suitable form to construct scattering diagrams. The procedure is described in

detail in ref 24. In what follows, only the most salient points are presented.

The kinetic energies of the projectile, T_p, and of the product ion, T'_p, define the energy gain/loss $\Delta T = T'_p - T_p$. From the measured energy gain ΔT, the laboratory collision energy T_p, and the laboratory scattering angle θ, the Q value or the net change in the total kinetic energy of the colliding system is given by[24]

$$Q = \frac{M}{m_t}\Delta T + 2\frac{m_p}{m_t}\left[1 - \left[1 + \frac{\Delta T}{T_p}\right]^{1/2}\cos\theta\right]T_p \quad (1)$$

where m_p and m_t are the masses of the projectile and target, respectively, and $M = m_p + m_t$. The scattering angle θ in the laboratory is related to the scattering angle Θ in the c.m. system by

$$\tan\theta = \frac{\sin\Theta}{\gamma + \cos\Theta}, \quad \text{where } \gamma = \frac{m_p}{m_t}\left(1 + \frac{MQ}{m_tT_p}\right)^{-1/2}$$

$$\left(\text{If } \frac{MQ}{m_tT_p} \ll 1 \text{ and } m_p = m_t, \gamma \approx 1 \text{ and } \theta \approx \Theta/2.\right)$$

The Q value is an invariant quantity which is the same in the laboratory and c.m. systems.

In low-energy scattering experiments, the results are most conveniently presented as an intensity or flux contour map on a standard Newton diagram.[26] In this velocity space, the product ion abundances are represented by a function $P_L(v,\theta)$. $P_L(v,\theta)$ is the relative probability of finding a scattered particle with velocity v and $v + dv$ and laboratory angle θ between θ and $\theta + d\theta$. It is related to the usual doubly differential cross section $I(v,\theta)$ by $P_L(v,\theta) = I(v,\theta)\sin\theta$. The two-dimensional Cartesian density plot can then be used to obtain a number of dynamical quantities such as the differential cross sections in the c.m. frame, the relative translation energy distribution of products $P(T')$, where T' is the relative final translational energy in the c.m., or the ratios of integral cross sections for different processes of interest.

For example, from $P(T') dT' = P(u_p) du_p$, where u_p is the product velocity in the c.m., we get

$$P(T') = \frac{du_p}{dT'}\int P(u_p,\Theta)\, d\Theta =$$

$$\frac{m_t}{m_pM}u_p\int P_C(u_{px},u_{py},u_{pz})\sin\Theta\, d\Theta \quad (2)$$

for the product relative translational final energy distribution. From $P(Q) dQ = P(T') dT'$, we have that $P(Q) = P(T')$, since $Q = T' - T$ and T, the relative initial translational energy in the c.m., is constant.

Since $\sigma_{tot} = 2\pi\int P_L(v,\theta)\, dv\, d\theta$, we can define $F_L(v,\theta)$ to be $2\pi P_L(v,\theta)/\sigma_{tot}$, in which case $\int F_L(v,\theta)\, dv\, d\theta = 1$. Thus by suitable normalization of the experimentally measured angular or angular and energy distribution functions, together with measured absolute total cross sections, one can get absolute values of singly or doubly differential cross sections.

Results

We have measured the angular distribution or scattering pattern of $Ar^{(q-1)+}$ products in Ar^{q+} ($11 \leq q \leq 14$) on Ar collisions at $72.4q$ eV projectile energy. In addition both angular and energy gain data were recorded. For all projectile charge states, q, the scattered $(q - 1)$ product intensity was observed at laboratory angles smaller than 5°. For all systems investi-

Single Charge Transfer in Ar^{q+} on Ar Collisions

J. Phys. Chem., Vol. 99, No. 42, 1995 **15671**

gated, the angular distributions are totally asymmetrical with respect to the center of mass of the colliding particles. The observed scattering patterns are typical of direct reaction mechanisms, in this case electron capture.

Since the scattering behavior of the even charge state projectiles is similar but different from that of the odd charge state projectiles, the results are grouped together according to the handedness of the projectile charge states. Parts a and b of Figure 2 show the scattering diagram and its corresponding three-dimensional representation for the Ar^{10+} product in Ar^{11+} on Ar collisions. In Figure 2a, the elliptical contours on the left represent the angular and velocity spread of the projectile beam. The figure is plotted in terms of the c.m. scattering angle in degrees and the c.m. velocity in meters per second. The 0° angle corresponds to the direction of the incident relative velocity vector. Since the scattering is cylindrically symmetric about the 0° axis, only half of the scattering diagram is shown. The full line contours connect points with the same value of relative scattering probability $P_L(v,\theta)$, while the dashed lines show extrapolated values. The value of 10 in $P_L(v,\theta)$ is arbitrarily assigned to the most intense feature in the energy gain spectrum at the scattering angle for which the scattered intensity is maximum. The scattering diagram for the Ar^{10+} product in Ar^{11+} on Ar shows only one peak with its maximum lying along the incident relative velocity vector. The diagram shows small contributions at the foot of the main peak (with relative intensities 0.4 and 0.3, respectively) and a wide but weak ridge at higher velocities.

Figure 2b shows a three-dimensional plot of the scattering diagram in part a. The data were reflected through a plane containing the incident relative velocity vector and perpendicular to the (v,θ) plane. To construct this 3-D representation, which gives the full picture of the section through velocity space, $P_L(v,\theta)$ was transformed into $P_L(v_x,v_y)$ with the x-axis parallel to the incident ion velocity.

Similar scattering patterns are shown in Figure 3 for the Ar^{12+} product in Ar^{13+} on Ar collisions. The main maximum again lies along the incident relative velocity vector. The weaker peaks with relative intensities of ~0.55 and ~0.3 at the foot of the main peak are less pronounced. A higher energy gain contribution has a broad angular distribution with a relative value of 0.1.

For even projectile charge states, the scattering diagram for the Ar^{11+} product in Ar^{12+} on Ar collisions is plotted in Figure 4a, and its three-dimensional representation is shown in Figure 4b. From Figure 4a it is clear that the scattering pattern is more complicated than that for the odd projectile charge states discussed above. Instead of only one peak, one peak and two distinct ridges are present. The first peak, which corresponds to the lowest energy gain products, has a maximum along the incident relative velocity vector. The first ridge peaks at about 1.75°. The ridge has considerable intensity at 0°, with a partially resolved maximum of about 8.7. The second ridge, which corresponds to the highest energy gain Ar^{11+} products, has an even wider angular distribution with two maxima. The first maximum with $P_L(v,\theta) \approx 2.9$ is at 4.4°, while the second one with $P_L(v,\theta) \approx 2$ is at 0°. Figure 4b is a 3-D representation of the scattering diagram in part a, together with its mirror symmetry generated complement. (The symmetry of the scattering pattern was confirmed experimentally in other but similar collision systems.[20])

Figure 5 shows a comparable picture for the Ar^{13+} scattered product in Ar^{14+} on Ar collisions. The scattering diagram (Figure 5a) again shows one peak and two distinct ridges. Due to the higher projectile charge state, the kinetic energy is higher
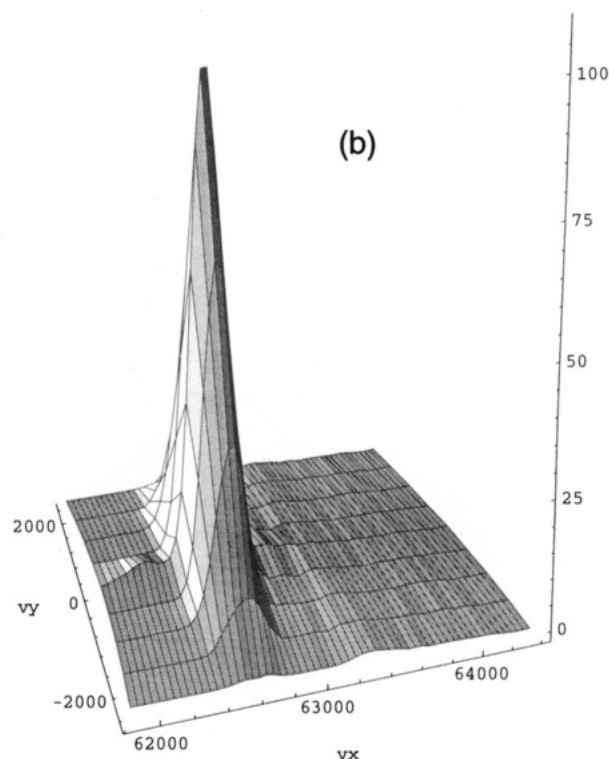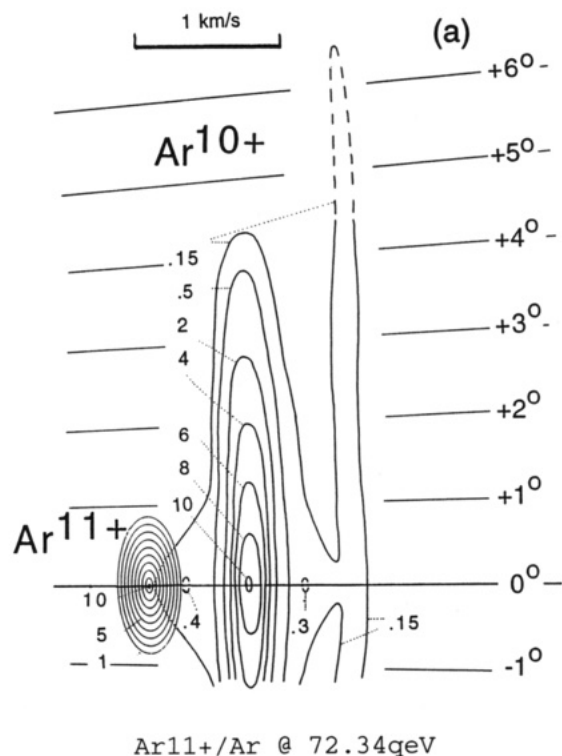

Figure 2. (a) Scattering diagram (contour density plot $P(u'_p,\Theta)$) for the Ar^{11+} on Ar collision system at $72q$ eV projectile laboratory energy. The contours, normalized to 10, are proportional to the reaction probability of the Ar^{10+} product ion being scattered into a center-of-mass scattering angle Θ with a given energy gain expressed in terms of velocity, bottom scale. The incident Ar^{11+} projectile beam contour, obtained from measured beam characteristics, shows the experimental angular and velocity spread. (b) 3-D visualization of the velocity distribution of Ar^{10+} products in Ar^{11+} on Ar collisions at $72q$ eV. v'_{p_x} and v'_{p_y} are the Cartesian components of the laboratory velocity vector $\mathbf{v}'_p$ in meters per second. The intensity along the z-axis is in arbitrary units.

and the resolution slightly lower. In this case, the first peak and the first ridge are not entirely resolved. Nevertheless, the
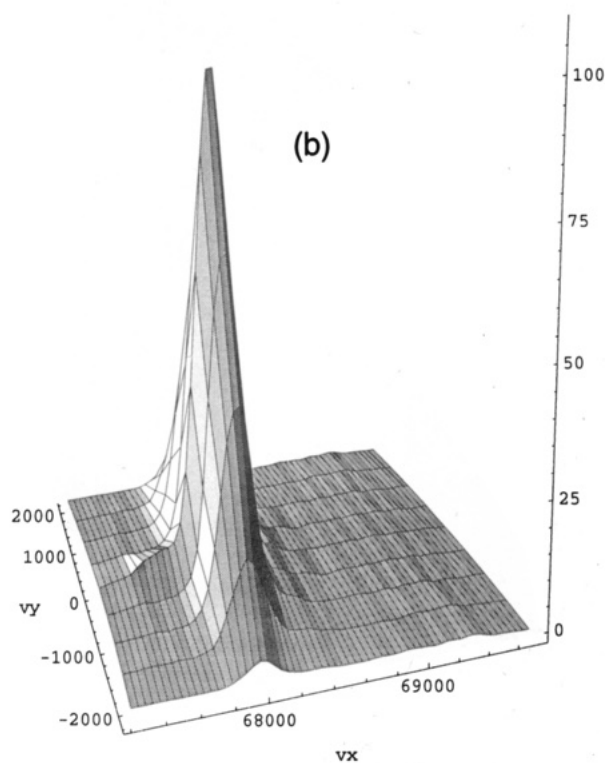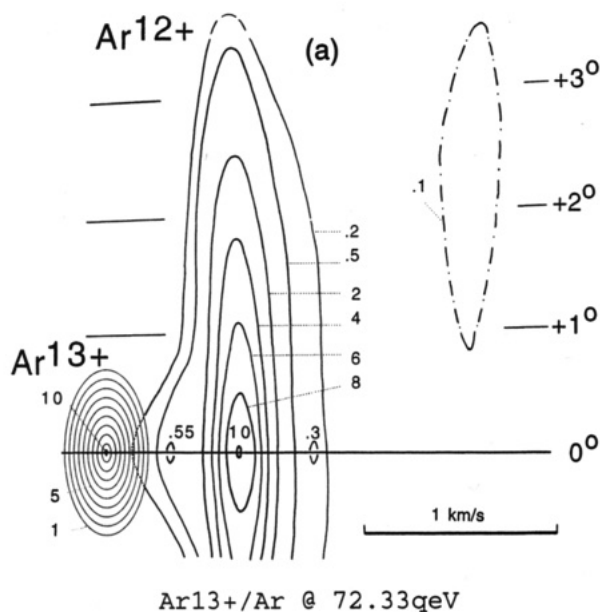
15672 *J. Phys. Chem., Vol. 99, No. 42, 1995*

Sadilek et al.

Figure 3. (a) Scattering diagram for Ar^{12+} products in Ar^{13+} on Ar collisions at $72q$ eV projectile laboratory energy. (b) 3-D representation of the scattering diagram in part a.

Figure 4. (a) Scattering diagram for Ar^{11+} products in Ar^{12+} on Ar collisions at $72q$ eV projectile laboratory energy. (b) 3-D representation of the scattering diagram in part a.

scattering pattern is similar to those observed with Ar^{12+}, Ar^{10+}, and Ar^{8+} projectiles.[20] The first peak which appears as a shoulder on the first ridge has a maximum $P_L(v,\theta)$ of ≈ 8. The ratio of the two maxima on the first ridge has changed, probably due to the higher collision energy. The peak at $\sim 1.8°$ is slightly smaller ($P_L(v,\theta) \approx 9.4$) than the peak at $0°$ ($P_L(v,\theta) \approx 10$). The second ridge has peaks at $3.55°$ with $P_L(v,\theta) \approx 2.6$ and at $0°$ with $P_L(v,\theta) \approx 1.7$. The latter is somewhat narrower than the former. The full 3-D representation of the scattering diagram of the Ar^{13+} product in Ar^{14+} on Ar collisions is shown in Figure 5b.

Figure 6 shows the relative, normalized to 1.0, c.m. angular distributions (differential cross sections dσ/dθ) of argon projectiles which retain one electron following the capture of one
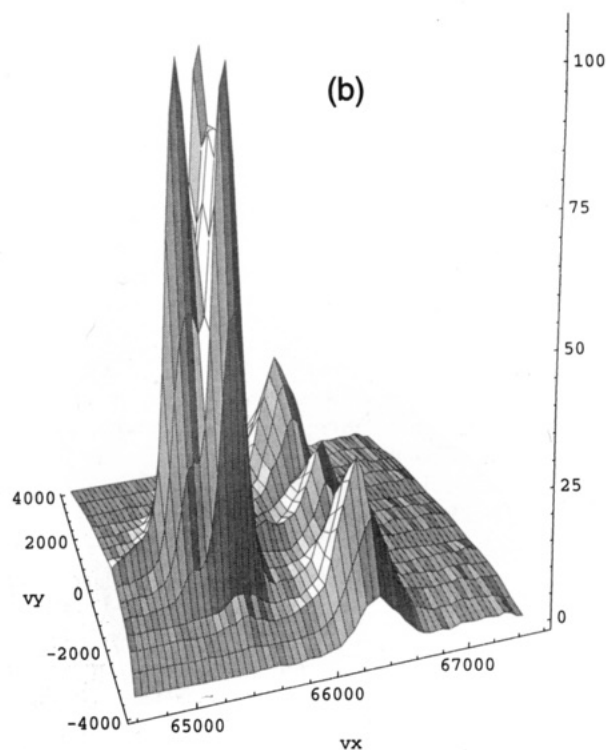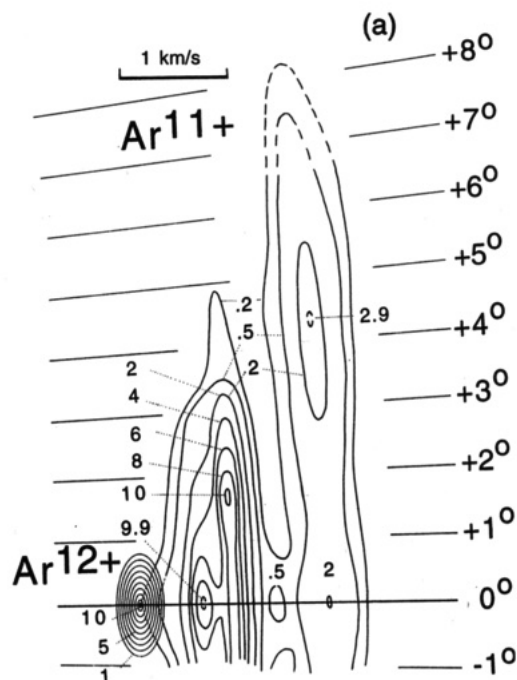
or more electrons from the target in Ar^{q+} ($11 \leq q \leq 14$) on Ar collisions at $72q$ eV. The difference in the distributions between odd (triangles) and even (circles) projectile charge states is clearly visible. In addition, within a group of odd or even projectile charge states, the angular distributions are quite similar. The narrowing of the angular distributions with increasing projectile charge state is most likely due to increasing projectile collision energy for a fixed deceleration potential, assuming $E\theta$ is constant. The odd projectile charge state angular distributions fall off monotonically with increasing angle, while, for the even projectile charge states, there is a slight increase in scattered intensity at about $1.75°$ c.m..

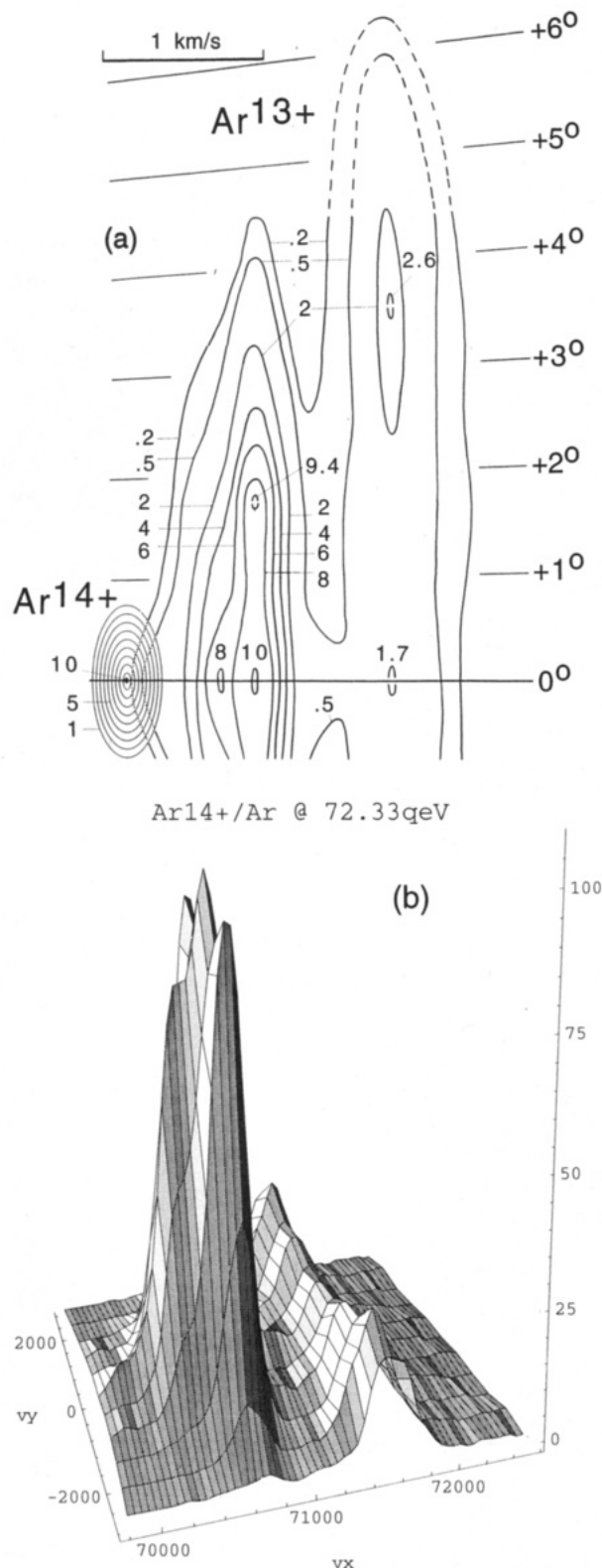By integrating the c.m. distributions $P_L(v,\theta)$ over the scat-

Single Charge Transfer in Ar^{q+} on Ar Collisions

J. Phys. Chem., Vol. 99, No. 42, 1995 **15673**

Ar14+/Ar @ 72.33qeV

Figure 5. (a) Scattering diagram for Ar^{13+} products in Ar^{14+} on Ar collisions at 72q eV projectile laboratory energy. (b) 3-D representation of the scattering diagram in part a.

tering angle θ (eq 2), we get $P(T')$ and hence $P(Q)$, the Q value distribution. Figure 7 shows the relative Q value distributions $P(Q)$ vs Q of the Ar$^{(q-1)+}$ products in Ar^{q+} on Ar collisions. For Ar^{11+} on Ar collisions, the maximum in the relative $P(Q)$ distribution occurs at 17.5 eV with much smaller Q value contributions around 35 eV. For Ar^{13+} on Ar, the most likely scattered projectile energy gain occurs at a Q value of 19 eV with minor contributions at 30 and 57 eV. The shapes of the
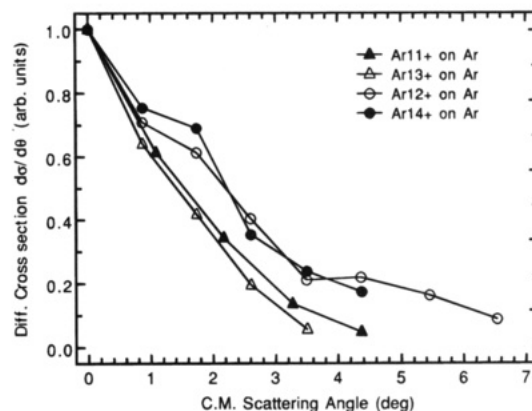

Figure 6. c.m. angular distributions of Ar$^{(q-1)+}$ products in Ar^{q+} on Ar collisions at 72q eV: filled triangles, Ar^{11+}; open circles, Ar^{12+}; open triangles, Ar^{13+}; filled circles, Ar^{14+}.
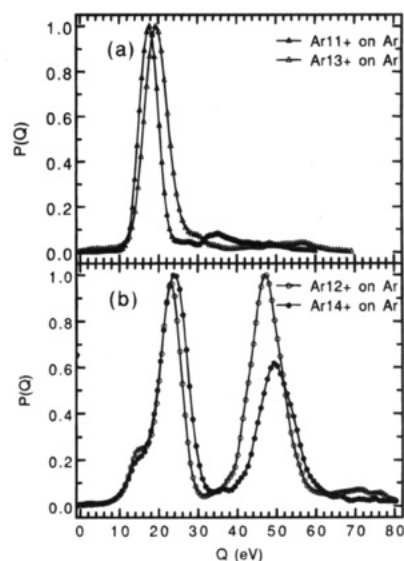

Figure 7. Q value distributions $P(Q)$ vs Q integrated over the scattering angles: (a) for odd projectile charge states Ar^{11+} and Ar^{13+} on Ar and (b) for even projectile charge states Ar^{12+} and Ar^{14+} on Ar.

two $P(Q)$ distributions for the odd projectile charge states are similar (Figure 7a).

Figure 7b shows the plot of $P(Q)$ vs Q for even charged argon projectiles. The first peak in the scattering diagram along the direction of the incident relative velocity vector (Figures 4a and 5a) is responsible for the lowest Q value, the almost resolved first peak in the figure at $Q \sim 15$ eV. The highest peak corresponds to the first ridge in the scattering diagrams along the same direction, with Q values of 23 eV for Ar^{12+} and 24 eV for Ar^{14+}. The height of the second ridge changes significantly from Ar^{12+} to Ar^{14+}, and the maxima in the $P(Q)$ vs Q distribution are at 47 and 50 eV, respectively. For Ar^{12+}, the intensity of the peak is due to the large angular range of the corresponding ridge in the scattering diagram, which is further enhanced by the sin θ weighting factor in the integration procedure (eq 2). The peaks at lower energy gains or Q values around 15−25 eV are most likely associated with single-electron capture. The higher Q values can be associated with transfer ionization involving multiple capture of r electrons ($r \geq 2$) followed by the ejection of ($r - 1$) electrons.

Discussion

The results of the current measurements are in good agreement with our previously measured 0° energy gain spectra.[21,22] The minor differences in the relative intensity of the observed
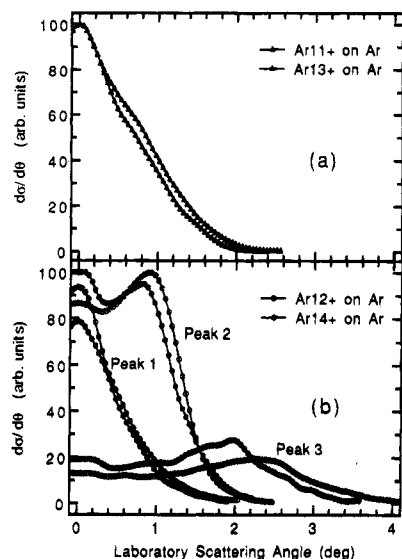
Figure 8. (a) Laboratory angular distributions of the $Ar^{(q-1)+}$ products in odd charge state projectiles Ar^{11+} (filled triangles) and Ar^{13+} (open triangles) on Ar. These distributions correspond to the single peak observed in the odd projectile charge state energy gain spectra. (b) Laboratory angular distributions of the $Ar^{(q-1)+}$ products in even charge state projectiles Ar^{12+} (open circles) and Ar^{14+} (filled circles) on Ar. The distribution labeled 1 is associated with the lowest energy peak in the energy gain spectra, 2 is associated with the second peak, and 3 is associated with the third.

energy gain peaks are probably due to the different collision energies and angular acceptances in the two experiments. We have verified that there is a consistent even–odd projectile charge state variation in both the energy gain and angular distribution data. While differences between the even and odd projectile charge state data are quite noticeable, there is a marked similarity among the data for a given handedness of projectile charge state. Figure 8 shows the laboratory angular distributions of the $(q - 1)+$ scattered argon projectile in Ar^{q+} on Ar collisions, grouped according to the handedness of the projectile charge state, part a for odd and part b for even. In Figure 8b, angular distributions associated with the three observed energy gains or Q values are shown separately. The angular distribution labeled Peak 1 corresponds to the lowest energy gain peak in the scattering diagram (Figures 4a and 5a). That labeled Peak 2 corresponds to the next value, and Peak 3 corresponds to the highest energy gain in the same figures. The similarity of the angular distributions within the odd or even projectile group is quite evident. The smaller angular spread for the higher projectile charges is due to the greater kinetic energy of the projectile, which increases by 13/11 and 14/12, respectively, for the consecutive odd and even charge states at the same decelerating potential.

In energy gain spectra involving lower charge argon projectiles ($6 \leq q \leq 10$) the distinct peaks observed are attributed to single-electron capture.[27,28] If this is the case for the higher projectile charges in the present experiment, then for Ar^{11+} and Ar^{13+} on Ar, the Coulomb barrier model[29,30] predicts capture into $n = 7$ with $Q = 21$ eV and into $n = 8$ with $Q = 23$ eV, respectively. For Ar^{12+} and Ar^{14+}, one gets $n = 7$ with $Q = 22$ eV and $n = 8$ with $Q = 24$ eV. These values are in reasonably good agreement with those shown in Figure 7a and the first large peaks in Figure 7b, given that the experimental uncertainty in the Q values is estimated to be ± 0.3 eV. For Ar^{12+} and Ar^{14+}, the small peak at $Q = 14$ eV corresponds to $n = 8$ and 9, respectively, if we take one-electron capture into a hydrogen-like state of the projectile with energy ϵ_n (a.u.). That is,

TABLE 1: *Q* **Values (in electronvolts) Associated with Possible Single- and Double-Electron Capture Quantum States**[a]

Single-Electron Capture Quantum States								
projectile charge	7s	7i	8s	8k	9s	9l	10s	10m
11+	21.0	17.8	12.9	10.0				
12+	27.3	24.3	16.9	14.8				
13+			22.0	20.2	13.9	12.6		
14+			27.5	25.9	18.3	17.2	11.7	10.9

Double-Electron Capture Quantum States								
projectile charge	$(6s)^2$	$(6p)^2$	$(7s)^2$	$(7p)^2$	$(8s)^2$	$(8p)^2$	$(9s)^2$	$(9p)^2$
11+	52.8	49.3	26.2	24.0				
12+	69.4	66.0	38.4	36.4	18.7	17.3		
13+			51.5	49.4	28.7	27.4	13.3	
14+			65.5	63.6	39.5	38.3	21.8	21.0

[a] The Q values were calculated according to eq 4 using total electronic energy values calculated with the help of the Hartree–Fock program MCHF-86.[31]

$$|\epsilon_n| = \frac{q^2}{2n^2} = Q + \text{IP} \qquad (3)$$

where IP is the first ionization potential of argon and q the projectile charge.

Q values for single-electron capture into different nl states of the projectile are given by

$$Q = \{E_{tot}(Ar^{q+}) + E_{tot}(Ar)\} - \{E_{tot}(Ar^{q+} + (nl)) + E_{tot}(Ar^+)\} \qquad (4)$$

where $E_{tot}(Ar^{q+})$ is the total electronic energy of the Ar^{q+} projectile, $E_{tot}(Ar)$ that of the argon atom, and so on. With the help of the Froese-Fischer Hartree–Fock program MCHF-86,[31] we have calculated Q values for a number of single-electron capture states for the different projectile charges. The results are summarized in Table 1. For Ar^{11+}, the single peak at $Q = 18$ eV could be due to capture to $7l$ states, since the Q values bracketed by $7i$ to $7s$ range from 17.8 to 21.0 eV. Similarly, the single peak at $Q = 19.5$ eV for Ar^{13+} is most likely due to capture to the $8l$ states of the projectile. For Ar^{12+}, the small peak at about 13 eV and the large peak at 23 eV are consistent with capture to the high angular momentum states with $n = 8$ and $n = 7$, respectively. For Ar^{14+}, one might expect capture into the high angular momentum states with $n = 8$ and $n = 9$, although the small peak around 15 eV is too low in energy to correspond to $n = 9$, $l = 8$.

It has been known for some time that true single-electron capture is responsible for less than half of the projectiles which end up with charge $(q - 1)+$. Multielectron capture processes, in which r electrons are captured and $r - 1$ are subsequently ejected contribute significantly to the total one-electron transfer cross section.[25,32] The higher Q values observed which appear as a broad peak in the translational energy spectra are commonly associated with these processes. However, definite identification of the specific multielectron capture states responsible for these energy gains is difficult to make because of the large number of possible states involved.

We consider next the angular distributions. In principle, these can be calculated semiclassically and compared with measured distributions. A semiclassical trajectory calculation combined with the multichannel Landau–Zener formalism for the probability of a collision ending up in a given final channel was applied to low-energy highly charged ion–atom scattering by

Single Charge Transfer in Ar^{q+} on Ar Collisions

J. Phys. Chem., Vol. 99, No. 42, 1995 **15675**

Andersson et al.[11] In a later paper, a more extensive calculation of angular distributions involving seven channels was carried out for 20−400 eV Ar^{4+} on Ar collisions.[13] It is also possible to calculate angular distributions or differential cross sections, total cross sections, and Q values within the framework of the molecular Coulomb barrier model according to a method proposed by Niehaus.[33] Either approach, semiclassical trajectories combined with the multichannel Landau−Zener formalism, or the molecular Coulomb barrier model, can be used to generate scattering diagrams. We briefly describe how such a calculation can be carried out within the framework of the semiclassical trajectory formalism.

Suppose that r electrons are captured by a projectile of charge q at a projectile−target separation $R = R_c$. We make the usual approximation that $V_{in}(R) = 0$ in the incoming channel. The deflection function χ for the path characterized as incoming on V_{in} to the capture radius R_c, incoming on $V_{out}(R) = r(q - r)/R - Q$ from R_c to the turning point, and outgoing on V_{out} from the turning point to infinity is

$$\chi(u_c) = -\sin^{-1}(u_c) + \sin^{-1}\left\{\frac{u_c^2 + (\kappa/2)}{[u_c^2(1 + \kappa) + (\kappa/2)^2]^{1/2}}\right\} + $$
$$\sin^{-1}\left\{\frac{\kappa/2}{[u_c^2(1 + \kappa) + (\kappa/2)^2]^{1/2}}\right\} \quad (5)$$

where $\kappa = r(q - r)/(u_c R_c E)$, E is the c.m. energy, and u_c ($0 \leq u_c \leq 1$) is the normalized impact parameter b/R_c. (Similar analytic expressions can be obtained for the other possible paths in this and the many final channel case.) Since $V_{out}(R_c) = r(q - r)/R_c - Q = V_{in}(R_c) = 0$, we also have $\kappa u_c = Q/E$. If the impact parameter $b = R_c$, then $u_c = 1$, and $\kappa = r(q - r)/R_c E = Q/E$. For $Q \ll E$, we get

$$\chi_c \equiv \chi(1) \approx \frac{r(q - r)}{2R_c E} \approx \frac{Q}{2E} \quad (6)$$

χ_c or $Q/2E$ is called the "Coulomb half-angle". It is determined at a given collision energy either by the number of electrons captured, r, and the capture radius, R_c, or by the Q value.

Following ref 11, when many reaction paths k lead to a final channel f, the differential cross section $d\sigma_f/d\Omega$ is given by

$$\frac{d\sigma_f}{d\Omega} = |\sum_k \left(P_f^k \frac{d\sigma_f^k}{d\Omega}\right)^{1/2} \exp(iA_f^k)|^2 \quad (7)$$

where $d\sigma_f^k/d\Omega$ is the classical differential cross section for transitions to the final channel f via path k, A_f^k is the classical action for path k, and P_f^k is a probability assigned to each path k. P_f^k is built up from the individual Landau−Zener probabilities p for remaining on a diabatic potential curve at each crossing. The Landau−Zener transition probabilities can be evaluated in the usual manner.[34] The classical differential cross section $d\sigma_f^k/d\Omega$ for the path k leading to the final channel f is obtained from the corresponding deflection function $\chi_f^k(b)$:

$$\frac{d\sigma_f^k}{d\Omega} = \frac{1}{\sin\theta}\sum_{b_j} b_j |\frac{d\chi_f^k}{db}|_{b_j} \quad (8)$$

where the summation is over all impact parameters b_j that satisfy the condition $\chi_f^k(b) = \theta$, where θ is the scattering angle.

For a collision system with a number of possible Q values, Q_f, $d\sigma_f/d\Omega$, and σ_f have to be calculated. These quantities

together with the possible Q values can then be used to construct the scattering diagram. The procedure is fairly tedious but straightforward for Q values associated with single-electron capture. However, for Q values corresponding to true multi-electron capture, it is not possible to calculate the P_f^k's, since the matrix elements in the expressions for the Landau−Zener transition probabilities p for remaining on the same diabatic potential curve are not known in this case. One would therefore expect that a calculation of the scattering diagram based on this approach could only be compared with the true one-electron capture portion of the measured scattering diagram. A calculation based on the molecular Coulomb barrier model has no unknown quantities. In this case a comparison with the experimental scattering diagram could be used to test the molecular Coulomb barrier model to see how well it predicts the Q values and angular distributions simultaneously. To our knowledge, such a calculation has not been done to date.

Angular distributions of charge-changed projectiles in coincidence with recoil ion charge states[17−19] show that the distributions extend to larger angles as the number of electrons captured from the target by the projectile increases. In our data, we observed that the scattered $(q - 1) +$ projectiles exhibit distinctly different angular distributions depending upon the energy gain. Therefore, it seemed reasonable to associate the lowest Q value peaks in Figure 4 with true single-electron capture, since the scattered projectiles had the smallest angular spread. The ridge at $Q \approx 23$ eV, corresponding to scattered projectiles with a greater angular spread was then thought to be made up of at least two components. The component centered along the relative velocity vector was associated with true one-electron capture, and the other, which peaks at about 1.7° c.m. (Figure 4a), was associated with two-electron capture. However, in subsequent experiments (unpublished) we have shown that if one looks at the time of flight spectrum of recoil ions in coincidence with $(q - 1)+$ projectiles that have undergone a specific energy gain, the two sharp peaks in the even projectile energy gain spectra and the single large peak in the odd projectile spectra indeed correspond to one-electron capture only. That is, the recoil ion spectrum shows only singly charged recoils. In the time of flight spectra of recoil ions in coincidence with the energy gain corresponding to the maximum in the "transfer ionization" peak (at ~50Q eV in all the spectra), one observes mostly doubly charged recoils. Thus the different angular distributions of the two sharp peaks in even projectile spectra are most probably due to the location of the crossing radii involved and the pertinent probabilities $P_f^k(b)$.

Finally, it is interesting to note the following, which we illustrate for Ar^{12+} on Ar collisions, although it appears to be true for the other even projectile charge states. If we take the shape of the measured angular distribution associated with $Q = 15$ eV (Peak 1 open circles in Figure 8b) and normalize it at $\theta = 0°$ to that associated with $Q \approx 23$ eV (Peak 2 open circles in Figure 8b) and then subtract the normalized Peak 1 from Peak 2, we get the curve shown in Figure 9 with filled squares. If we then take the same Ar^{12+} on Ar Peak·1 curve, redrawn with open circles in Figure 9, and normalize it at 0° to the angular distribution of the single peak observed in Ar^{11+} on Ar collisions (filled triangles in Figure 9) and then subtract the former from the latter, we get the peak shown by the open squares in Figure 9. This peak is almost identical in shape to that obtained above if the shape of the angular distribution corresponding to $Q = 15$ eV is subtracted from that corresponding to $Q \approx 23$ eV in Ar^{12+} on Ar collisions (filled squares in Figure 9). The two subtracted peaks are shown on the same scale in Figure 9 in order to display their similarity.
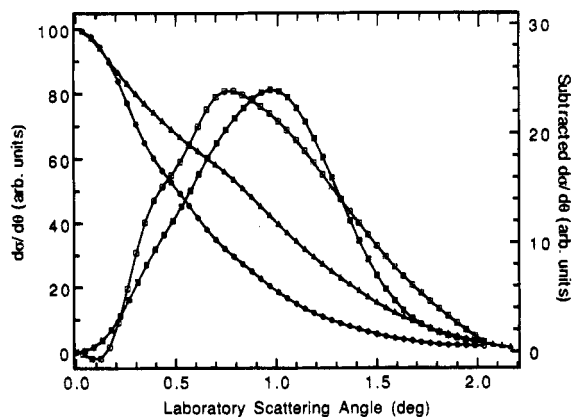
Figure 9. Left hand scale: Angular distribution of the single peak observed in the Ar^{11+} on Ar energy gain spectrum (filled triangles) and that of the lowest energy peak in the Ar^{12+} on Ar energy gain spectrum (open circles). Both peaks are normalized to 100. Right hand scale: Angular distribution (open squares) of the lowest energy peak in the Ar^{12+} on Ar energy gain spectrum (open circles) subtracted from the angular distribution of the single peak in the Ar^{11+} on Ar energy gain spectrum (filled triangles). This peak is very similar in shape to that obtained when the properly normalized angular distribution of the energy gain peak corresponding to $Q = 15$ eV is subtracted from the angular distribution of the energy gain peak corresponding to $Q \approx 23$ eV in Ar^{12+} on Ar collisions (filled squares).

While one might question the subtraction procedure, the angular distributions of the other even projectile charge states exhibit the same behavior when subjected to this procedure. Therefore, one might conclude that the single peak observed in odd charge projectile energy gain spectra consists of unresolved components whose angular distributions are similar to those obtained for the resolved components observed with even charge projectiles.

The appearance of the $P(Q)$ vs Q distributions for the one-electron transfer process (Figure 7), which is different, depending upon whether the projectile charge state is even or odd, is quite puzzling. We have no explanation for this effect at present. The Q value distribution should reflect the density of electron capture states, and we see no obvious reasons why this should depend on the handedness of the projectile charge. In Figure 7a, the intense peak is due to single-electron capture, as is the first peak in part b. The second peak in Figure 7, which is small for the odd and large for the even projectile charges, is mostly due to two-electron capture. One-electron transfer accounts for more than 80% of the total cross section and seems to consist almost entirely of one-electron and some two-electron capture from the target. However, measured total and one- and two-electron transfer cross sections[25,32] are fairly independent of the projectile charge state and show no marked even−odd variations. It is true that the angular distribution and energy gain measurements in this work were done at collision energies below $100q$ eV whereas the total cross section measurements were carried out at $2.3q$ keV[25] and higher[32] collision energies. It is possible that one should not try to reconcile the lower energy differential cross sections with the total and transfer cross sections at higher energies and that the cross sections at the lower energies do show such oscillations. However, that is probably unlikely. Finally, two- and three-electron transfer, which is made up of capture of more than two electrons, is spread over larger scattering angles and higher Q values. Consequently, the intensity in a given angular and energy spread is quite low, and investigation of these processes will require a different approach than taken in these experiments.

Summary

We have measured angular and energy gain distributions of single-electron transfer products in collisions of highly charged Ar^{q+} ions ($11 \le q \le 14$) with Ar at $72q$ eV laboratory projectile energies. The even−odd variation in 0° energy gain spectra which was observed in a previous study[21,22] has also been observed in the scattering patterns. Odd charge state Ar^{q+} projectiles produce a single peak in scattering diagrams while even charge state projectiles exhibit a structure with three distinct components which differ significantly in their angular spread. The reason for the different shapes of the scattering diagrams for even and odd projectile charge states is not fully understood at this time. Using a deconvolution procedure, we can show that the odd charge state projectile scattering patterns consist of contributions of peaks shaped similarly to those observed for the even charge state projectiles. The contributions most probably originate from similar processes, but their relative weights differ for the odd and even projectile charge states.

References and Notes

(1) Vancura, J.; Friedrich, B.; Sadilek, M.; Herman, Z. *Chem. Phys. Lett.* **1985**, *120*, 243.

(2) Cocke, C. L.; Kamber, E. Y.; Tunnell, L. N.; Varghese, S. L.; Waggonner, W. *Nucl. Instrum. Methods Phys. Res.* **1987**, *A262*, 89.

(3) Barat, M.; Roncin, P.; Guillemot, L.; Gaboriaud, M. N.; Laurent, H. *J. Phys. B* **1990**, *23*, 2811.

(4) Keller, N.; Andersson, L. R.; Miller, R. D.; Westerlind, M.; Elston, S. B.; Sellin, I. A.; Biedermann, C.; Cederquist, H. *Phys. Rev. A* **1993**, *48*, 3684.

(5) Tunnell, L. N.; Cocke, C. L.; Giese, J. P.; Kamber, E. Y.; Varghese, S. L.; Waggonner, W. *Phys. Rev. A* **1987**, *35*, 3299.

(6) Roncin, P.; Barat, M.; Gaboriaud, M. N.; Laurent, H. *J. Phys. B* **1989**, *22*, 509.

(7) Roncin, P.; Barat, M.; Laurent, H. *Europhys. Lett.* **1986**, *2*, 371.

(8) Laurent, H.; Barat, M.; Gaboriaud, M. N.; Guillemot, L.; Roncin, P. *J. Phys. B* **1987**, *20*, 6581.

(9) Roncin, P.; Gaboriaud, M. N.; Barat, M.; Laurent, H. *Europhys. Lett.* **1987**, *3*, 53.

(10) Andersson, L. R.; Cederquist, H.; Barany, A.; Liljeby, L.; Biedermann, C.; Levin, J. C.; Keller, N.; Elston, S. B.; Gibbons, J. P.; Kimura, K.; Sellin, I. A. *Phys. Rev. A* **1991**, *43*, 4075.

(11) Andersson, L. R.; Pedersen, J. O. P.; Barany, A.; Bangsgaard, J. P.; Hvelplund, P. *J. Phys. B* **1989**, *22*, 1603.

(12) Andersson, L. R.; Cederquist, H.; Barany, A.; Liljeby, L.; Biedermann, C.; Levin, J. C.; Keller, N.; Elston, S. B.; Gibbons, J. P.; Sellin, I. A. *Phys. Rev. A* **1992**, *45*, R4.

(13) Biedermann, C.; Cederquist, H.; Andersson, L. R.; Levin, J. C.; Short, R. T.; Elston, S. B.; Gibbons, J. P.; Andersson, H.; Liljeby, L.; Sellin, I. A. *Phys. Rev. A* **1990**, *41*, 5889.

(14) Said, R.; Kamber, E. Y.; Yaltkaya, S.; Gopinathan, M.; Ferguson, S. M. *Nucl. Instrum. Methods in Phys. Res.* **1993**, *B79*, 40.

(15) Biedermann, C.; Levin, J. C.; Short, R. T.; Elston, S. B.; Gibbons, J. P.; Sellin, I. A.; Cederquist, H.; Andersson, L. R.; Andersson, H.; Liljeby, L. *Phys. Rev. A* **1990**, *42*, 6905.

(16) Biedermann, C.; Levin, J. C.; Short, R. T.; Elston, S. B.; Gibbons, J. P.; Kimura, K.; Keller, N.; Sellin, I. A.; Cederquist, H.; Andersson, L. R.; Andersson, H.; Liljeby, L. *Nucl. Instrum. Methods Phys. Res.* **1991**, *B56/57*, 74.

(17) Danared, H.; Andersson, H.; Astner, G.; Barany, A.; Defrance, P.; Rachafi, S. *J. Phys. B* **1987**, *20*, L165.

(18) Guillemot, L.; Roncin, P.; Gaboriaud, M. N.; Laurent, H.; Barat, M. *J. Phys. B* **1990**, *23*, 4293.

(19) Ali, R.; Cocke, C. L.; Raphaelian, M. L.; Stockli, M. *J. Phys. B* **1993**, *26*, L1.

(20) Vancura, J.; Sadilek, M.; Kostroun, V. O. Submitted to *Phys. Rev. A*.

(21) Vancura, J.; Kostroun, V. O. VIth International Conference on the Physics of Highly Charged Ions, AIP Conference Proceedings 274; Richard, P., Stockli, M., Cocke, C. L., Lin, C. D., Ed.; American Institute of Physics: New York, 1993; p 117.

Single Charge Transfer in Ar^{q+} on Ar Collisions

J. Phys. Chem., Vol. 99, No. 42, 1995 **15677**

(22) Vancura, J.; Kostroun, V. O. Submitted to *Phys. Rev. A*.

(23) Kostroun, V. O. *Proceedings of the International Symposium on Electron Beam Ion Sources and their Applications*, AIP Conference Proceedings 188; Hershcovitch, A., Ed.; American Institute of Physics: New York, 1989; p 65.

(24) Vancura, J.; Perotti, J. J.; Flidr, J.; Kostroun, V. O. *Rev. Sci. Instrum.* **1993**, *64*, 3139.

(25) Vancura, J.; Perotti, J. J.; Flidr, J.; Kostroun, V. O. *Phys. Rev. A* **1994**, *49*, 2515.

(26) Levine, R. D.; Bernstein, R. B. *Molecular Reaction Dynamics and Chemical Reactivity*; Oxford University Press: New York, 1987.

(27) Nielsen, E. H.; Andersen, L. H.; Barany, A.; Cederquist, H.; Heinemeier, J.; Hvelplund, P.; Knudsen, H.; MacAdam, K. B.; Sorensen, J. *J. Phys. B* **1985**, *18*, 1789.

(28) Giese, J. P.; Cocke, C. L.; Waggonner, W.; Tunnell, L. N.; Varghese, S. L. *Phys. Rev. A* **1986**, *34*, 3770.

(29) Ryufuku, H.; Sasaki, K.; Watanabe, T. *Phys. Rev. A* **1990**, *21*, 745.

(30) Niehaus, A. *J. Phys. B* **1986**, *19*, 2925.

(31) Froese-Fischer, C. *Comput. Phys. Commun.* **1987**, *43*, 355.

(32) Ali, R.; Cocke, C. L.; Raphaelian, M. L. A.; Stockli, M. *Phys. Rev. A* **1994**, *49*, 3586.

(33) Niehaus, A. *J. Phys. (Paris)* **1987**, *C9*, 137.

(34) Olson, R. E.; Salop, A. *Phys. Rev. A* **1976**, *14*, 579.